Laser powder bed fusion of high-strength maraging steel with concurrently enhanced strength and ductility after heat treatments

Jun Song [a, b], Qian Tang [a, *], Hao Chen [c], Zhiqing Zhang [c], Qixiang Feng [a], Mingqiang Zhao [a], Shuai Ma [a], Rossitza Setchi [b]

a State Key Laboratory of Mechanical Transmissions, Chongqing University, Chongqing 400044, China

b Cardiff School of Engineering, Cardiff University, Cardiff CF24 3AA, UK

c College of Materials Science and Engineering, Chongqing University, Chongqing 400044, China

* Corresponding author: Qian Tang

Address: No. 174, Shazheng Street, Shapingba District, Chongqing 400044, China.

Telephone: +8613983664650

E-mail address: tqcqu@cqu.edu.cn

Abstract

Laser powder bed fusion (LPBF) has been demonstrated as a metal additive manufacturing technique that can manufacture high-performance metal components with complex shapes directly from raw powder materials. Although 18Ni-300 maraging steel has been extensively employed in this process, a significant trade-off has always existed between strength and ductility when using traditional solution and ageing heat treatments. This study addresses this problem by introducing a heat treatment combination that includes hot isostatic pressing (HIP) before the conventional ageing treatment. The experimental results demonstrated an enhancement of the relative density from 99.6 % in the as-built conditions to 99.96% after HIP, although a small number of residual gas pores remained. The subsequent ageing treatment after HIP had a negligible effect on the reopening of these closed defects. Microstructure observations revealed that a fully martensitic structure can be obtained after HIP, and austenite reversion was less sensitive with the HIP+ageing treatment (HAT) compared to direct

ageing treatment (DAT). Grain growth and alloying homogenisation also occurred during HIP. Massive nanoscale precipitations were formed both after DAT and HAT; quantitative analysis based on TEM observation indicated that the size of these precipitates was larger after subjecting to HAT. The room-temperature ultimate tensile strength and elongation to failure after HAT were approximately 6 % and 100% higher than DAT, confirming the simultaneous enhancement of the strength and ductility after HAT. The findings of the present study offer insights into heat treatment approaches that can overcome the strength-ductility trade-off of LPBF-manufactured 18Ni-300 maraging steel, while also providing an alternative strategy for obtaining the simultaneous improvement of strength and ductility through heat treatments.

Keywords: Laser powder bed fusion; maraging steel; hot isostatic pressing; mechanical behaviour; strengthening mechanism

1. Introduction

Laser powder bed fusion (LPBF) is a highly promising additive manufacturing technique that has received considerable attention in recent years [1]. One advantage of the LPBF technique is that it provides the possibility of manufacturing high-performance metallic components with complex structures directly from raw powders, layer by layer, which cannot be achieved using traditional manufacturing methods. Due to the intrinsic behaviours of rapid solidification and cooling (around 10^7 K/s) during LPBF, the LPBF-manufactured components without heat treatments often exhibit comparable or improved properties compared to traditionally manufactured components. After several decades of rapid development, extensive studies have demonstrated the use of LPBF for the manufacture of a variety of high-performance metal components, such as titanium alloys [2, 3], iron-based alloys [4], aluminium alloys [5], and nickel-based superalloys [6].

18Ni-300 maraging steel is a precipitation-hardening iron-nickel alloy commonly used in the automotive, aerospace and casting areas due to its high strength, excellent toughness and weldability [7]. Consequently, the use of LBPF to fabricate this high-performance alloy has become highly attractive in recent years. Previous studies that

have concentrated on 18Ni-300 maraging steels fabricated by LPBF have mainly focused on process optimisation, material microstructure and performance characterisation. For example, Casalino et al. [8] performed a statistical optimisation of 18Ni-300 maraging steel fabricated by LPBF and found that a relative density greater than 99% can be obtained with laser power greater than 90 W and scan speed less than 220 mm/s. Souza et al. [9] investigated the effect of critical process parameters on the manufacturing efficiency of 18Ni-300 maraging steel during LPBF and found that the layer thickness had a greater effect on the manufacturing speed than on the scan speed. Recently, Bai et al. [10] systematically studied the relationship between process parameters and surface quality of LPBF-manufactured 18Ni-300 maraging steel and found that the surface quality was reduced when using a low hatch spacing due to material aggregation induced by mass transfer during processing. In particular, they demonstrated that the volumetric energy density provides only limited predictions of surface quality.

The abovementioned literature suggest that LPBF is capable of producing nearly full dense 18Ni-300 maraging steel components using optimal process parameters. To tailor the microstructure and improve the mechanical performance, heat treatments have commonly been employed in LPBF-built 18Ni-300 maraging steel. Conventional heat treatments fall mainly into three categories: solution treatment, direct ageing and solution-ageing [11, 12]. Ultra-high strength can be obtained with appropriate ageing treatments due to the formation of massive nanoscale precipitations, such as Ni_3Ti, Ni_3Mo and Fe_2Mo during ageing [13, 14].

In recent years, researchers have performed extensive studies on the effect of these three heat treatments, using various temperatures and duration times, on the mechanical behaviours of LPBF-built 18Ni-300 maraging steels. For example, Kempen et al. [15] studied the effect of various ageing conditions on the mechanical properties of 18Ni 300 maraging steel by LPBF. Their samples had a UTS of 2217 MPa and hardness of 58 HRC after ageing at 480 for 5 h. Mutua et al. [16] studied the anisotropic behaviour of the build direction of LPBF-manufactured 18Ni-300 maraging steels and found lower tensile strength and elongation for vertically built than for horizontally built

samples.

Song et al. [12] and Tan et al. [17] compared the mechanical behaviours of the LPBF-manufactured samples under both solution-ageing and direct ageing treatments. They found that solution-aged conditions led to a degraded strength and improved ductility compared to aged materials. Tan et al. [17] also concluded that the combined solution-ageing treatment was preferable for LPBF-built maraging steels; however, Casati et al. [18] suggested that the solution treatment before ageing was not compulsory for obtaining ultra-high strength. The comprehensive study by Yin et al. [19] revealed changes in the microstructure and mechanical behaviours of LPBF-fabricated 18Ni-300 maraging steels under different ageing conditions. They found that the microstructure was less sensitive to the ageing holding time than to the temperature and that an optimal wear resistance behaviour was obtained after ageing at 490 °C for 3 h.

Previous research has focused mainly on the effect of traditional heat treatments on the mechanical behaviours of LPBF-fabricated 18Ni-300 maraging steel. However, the concurrent enhancement in strength and ductility of LPBF-built 18Ni-300 maraging steel still presents a challenge when using traditional heat treatments. Few studies have concentrated on overcoming this existing problem of the strength-ductility trade-off. Recently, Dehgahi et al. [20] introduced a higher content of elemental Ti in the raw powders to obtain a concurrent enhancement of the tensile strength and ductility of age-treated 18Ni-300 maraging steel; however, the increase in element Ti also increased the cost of the materials. Other approaches are needed to address this challenge.

One possibility is to use hot isostatic pressing (HIP). This is an effective post-processing method that plays an increasingly important role in mitigating the defects originally formed in LPBF-built components and improving their mechanical properties [21-23]. This process is also employed in conjunction with traditional heat treatments because this hybrid heat treatment can simultaneously improve the strength and ductility of LPBF-fabricated components [24]. However, to date, few studies have examined the potential of using this process with LPBF-manufactured 18Ni-300 maraging steels, and the influences on the microstructure and mechanical behaviours

also remain unclear.

To address the above knowledge gap, the present study is examined the feasibility of using the HIP process on 18Ni-300 maraging steel fabricated by LPBF. Specifically, the work compares the effect of direct ageing and combined HIP+ageing treatment on the microstructure and mechanical behaviours. The strengthening mechanisms of the mechanical behaviours in the direct ageing and HIP+ageing treatments are also discussed. The main purpose of this study is to offer preliminary evidence for the simultaneous improvement of the strength and ductility of LPBF-manufactured 18Ni-300 maraging steels using a combination of HIP and ageing heat treatment.

2. Experimental methods

2.1 Materials and sample preparation

Gas-atomised 18Ni-300 maraging steel powder, supplied by SLM Solutions Group AG, was employed as the raw materials. The alloying composition (wt.%) of the raw powder was 17.78Ni-8.99Co-4.93Mo-0.61Ti-0.19Al-0.02Mn-0.1Si-0.01P-0.17S-≤0.03C-Bal. Fe, as measured by inductively coupled plasma optical emission spectroscopy (ICP-OES, Agilent 5110, USA). The particle morphology showed that most powder particles were spherical (Fig. 1a). The particle size distribution, as measured with a Mastersizer 2000 (Malvern, UK), showed D10, D50 and D90 values of the powder of 19.04, 29.50 and 45.73 μm, respectively (Fig. 1b).

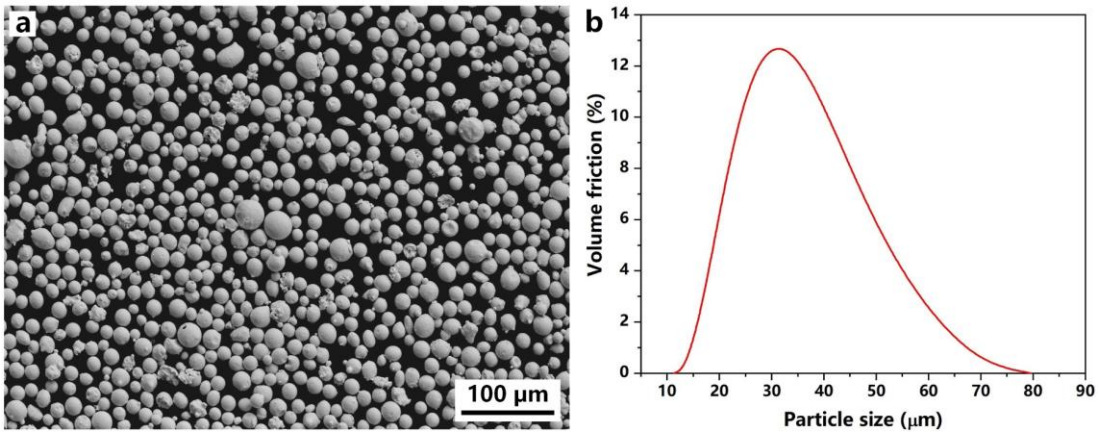

Fig. 1. The 18Ni-300 maraging steel feedstock used in this study: (a) SEM surface morphology; and (b) particle size distribution.

Both cubic samples with dimension size of 7 × 7 × 7 mm^3 and tensile samples were manufactured with an SLM Solutions 280 machine equipped with a continuous wave IPG fibre laser with a maximum power of 400 W and beam focus diameter of 80-115 μm. The process parameters that were provided by SLM solutions for the fabrications employed were: laser power of 200 W, scanning speed of 800 mm/s, hatch spacing of 0.12 mm and layer thickness of 0.03 mm. A stripe scanning strategy with a length of 6 mm was used with a rotation angle of 67˚ between adjacent layers, as shown in Fig. 2a. The 316 L stainless steel build plate was not preheated before manufacturing and the processing was performed under an Argon gas environment with an oxygen content lower than 1000 ppm to avoid oxidation. In addition, to guarantee dimension accuracy and surface quality of the samples, the contour strategy was also applied with process parameters: laser power of 100 W, scanning speed of 425 mm/s, border compensation of 0.05 mm and border distance of 0.08 mm.

2.2 Post-treatment processing

For post-treatment investigations, the as-built samples were subjected to three different post-treatment conditions: HIP, direct ageing and a combined HIP and ageing treatment. HIP was performed at 1050 ℃ and 150 MPa for 3 h under an argon atmosphere, followed by furnace cooling. For the ageing treatment, half of the as-built and HIP samples were processed at 500 ℃ for 6 h under a vacuum environment, followed by furnace cooling [25]. The detailed conditions are shown in Fig. 2b. Note that the direct ageing treatment and the combined HIP and ageing treatment are referred to DAT and HAT, respectively, hereafter in this study.

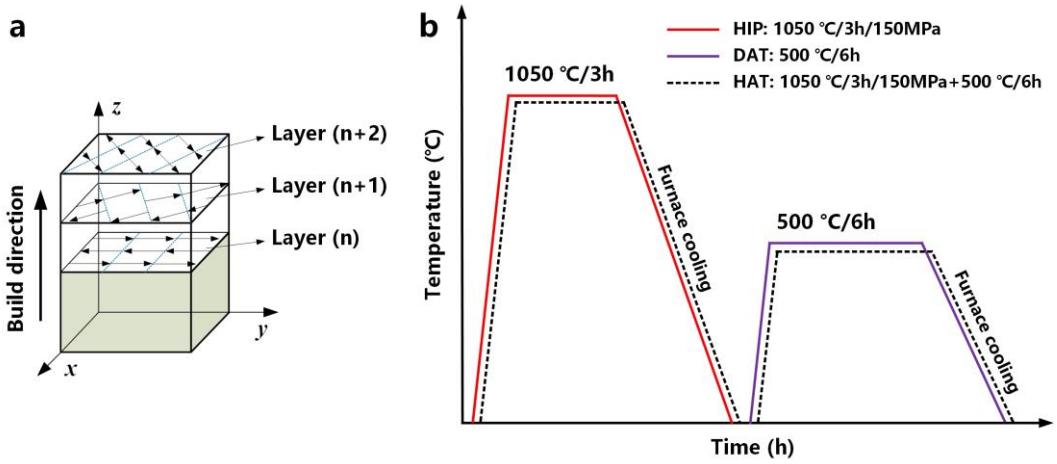

Fig. 2. Sketch of the (a) scanning strategy and (b) different heat treatments used in this study.

2.3 Material characterisation techniques

Density measurement was determined using the Archimedes method and an HZY-A120 electronic balance. The relative density of each sample was determined by taking an average value of five measurements. Samples were vertically sectioned and ground along the build direction by standard processing and then polished with 3 μm and 1 μm diamond polishing suspensions and 0.04 μm SiO_2 polishing suspensions before microstructure observations. Defects formed in the polished section were detected by optical microscopy (OM, Keyence VHX-1000 digital microscope, Japan). An X-ray microcomputed tomography (Micro-CT, Diondo d2, Germany) scanner was used for further investigations of the effect of different heat treatments on the porosity distribution in the samples with a volume of 2.5 × 2.5 × 2.5 mm^3 at 120 kV voltage and 100 μA with 5 μm voxel resolution.

To reveal the solidification boundaries and microstructures, the polished samples were etched using a solution consisting of 25 mL HNO_3, 50 mL HCl, 1 g $CuCl_2$ and 150 mL water, and then observed by scanning electron microscopy (SEM; JEOL JSM-7800F FEG, Japan). Before XRD and electron backscatter diffraction (EBSD) analysis, the polished samples were electropolished with a reagent of perchlorate and ethyl alcohol under 20 V at room temperature. Phase compositions were measured using a SmartLab XRD diffractometer with CuKα radiation at 40 kV and 40 mA at a scan speed

of 2°/min and a step size of 0.02°. The volume fraction of the austenite phase in different heat-treated conditions was quantitatively calculated based on the XRD results using the method reported by Wang et al [26].

The EBSD analysis was performed with an area of 400 × 400 μm^2 under 20 kV with a step size of 0.8 μm. The HKL Channel 5 EBSD software package was used to analyse the experimental data. Transmission electron microscopy (TEM) of the nanostructure was performed using an FEI TECNAI G20 instrument equipped with an energy-dispersive X-ray (EDX) system at 30 kV.

Uniaxial tensile tests were performed at room temperature on an electronic universal testing machine (Instron 5982, USA) with a loading speed of 2 mm/min based on the ISO 6892-1: 2019 standard. Three samples for each condition were tested to determine the average tensile strength. The fracture surfaces following tensile testing were observed using the JEOL JSM-7800F scanning electron microscope. Vickers microhardness was measured at room temperature using a Zwick tester at a constant load of 500 g with a dwell time of 8 s according to the ISO 3878: 1983 standard. To improve the accuracy and reliability of the results, average values for each sample were obtained from twenty different locations along the build direction on the polished surface.

3. Results

3.1 Relative density and defects

Fig. 3 shows the relative density of the samples in the as-built and post-treated conditions. The relative density of the as-built sample was measured as 99.6% when the optimal process parameters were applied. According to the figure, the measurements indicated that the DAT sample also exhibited an equivalent relative density, with a value 0.1% higher than that of the as-built sample. Compared to the as-built and DAT samples, the relative density increased after the samples were subjected to the HIP process. The measured relative density of the HIP sample was 99.96%. Subjecting the HIP sample to the aging treatment resulted in only a small decrease in relative density, to 99.93%. This result indicated that the HIP samples subjected to an

ageing treatment maintained almost a full relative density comparable to that of the HIP samples.

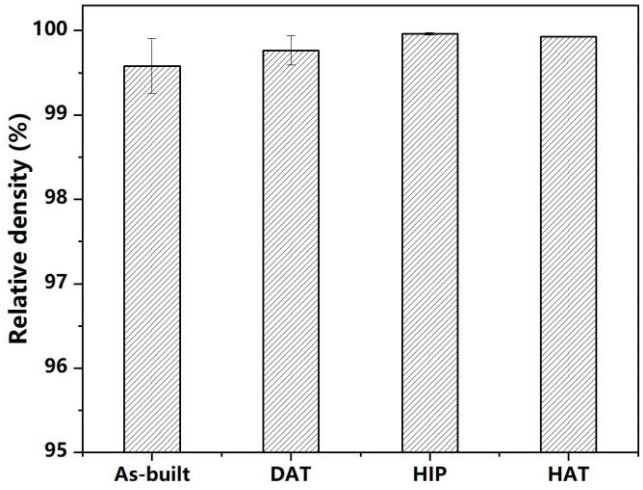

Fig. 3. Relative density measurements of the samples under different conditions.

Fig. 4 shows the optical micrographs of the defect distributions along the build direction in the as-built and heat-treated samples. The morphology shown in Fig. 4a indicates that only a limited number of small pores were detected in the as-built sample. These pores can be categorised into two different dominant types based on the pore morphology and size: gas pores and lack of fusions. The gas pores have near-spherical shapes and generally result from the argon atmospheric gas and entrapped pores from the original powders. By contrast, the lack of fusions arise due to the insufficient fusion between adjacent tracks and layers during processing [27]. When compared with the as-built sample, the DAT sample showed similar pore extent and morphology (Fig. 4b). As the OM observations show, residual gas pores were the primary defects in the HIP sample (Fig. 4c), suggesting that the employment of the HIP treatment could efficiently close most defects formed in the as-built condition. The number of residual gas pores in the HAT sample was slightly higher than that found in the HIP sample; however, the larger lack of fusions were not observed after ageing (Fig. 4d).

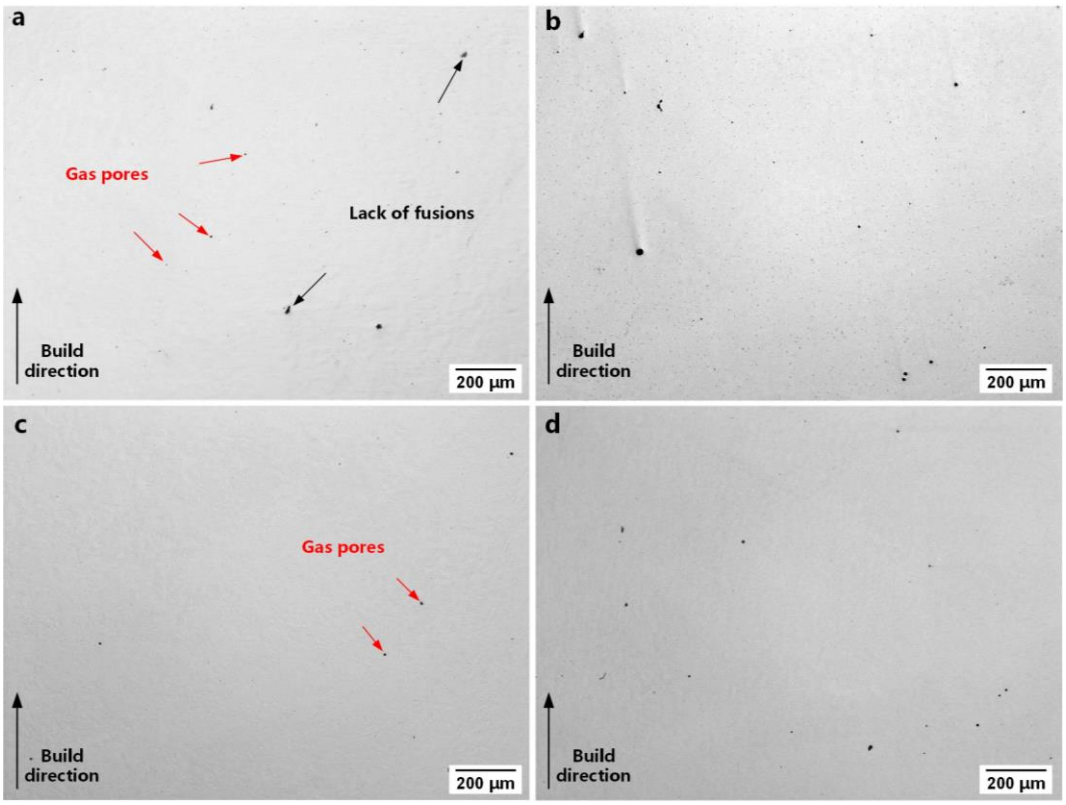

Fig. 4. Optical micrographs showing the defects in the vertical sections of the samples at different conditions: (a) as-built; (b) DAT; (c) HIP; and (d) HAT.

The differences in the defect distributions and morphologies arising from the various heat treatment conditions were further evaluated using reconstructed micro-CT images, as shown in Fig. 5. The observations were consistent with the optical micrograph measurements. The as-built and DAT samples showed similar defect morphologies and distributions, as well as uniform formation and distribution within the samples (Fig. 5a and b). The samples showed both gas pores and lack-of-fusion defects. The gas pores were smaller in size and nearly spherical, while the defects due to lack of fusion were irregular and larger. The quantitative analysis revealed approximately 2052 and 2464 defects in the as-built and DAT samples, respectively (0.0182% and 0.0246% in the volume fraction, respectively), and the equivalent diameters of the defects were smaller than 77 µm.

By contrast, the micro-CT observations confirmed a dramatic reduction in defects in the HIP and HAT samples (Fig. 5c and d). The figure shows that the majority of these

defects were spherical gas pores, whereas only a very small number were lack-of-fusion defects, and those were located close to the surface. The quantitative results revealed that the HIP sample had approximately 1365 defects (0.0044% in volume fraction), while the defect number was 1130 (0.0030% in volume fraction) after HAT. Most defects were smaller than 32.26 μm in equivalent diameter. These observations suggest that most defects formed during LPBF of 18Ni-300 maraging steel, especially lack of fusion defects, can be efficiently eliminated by HIP.

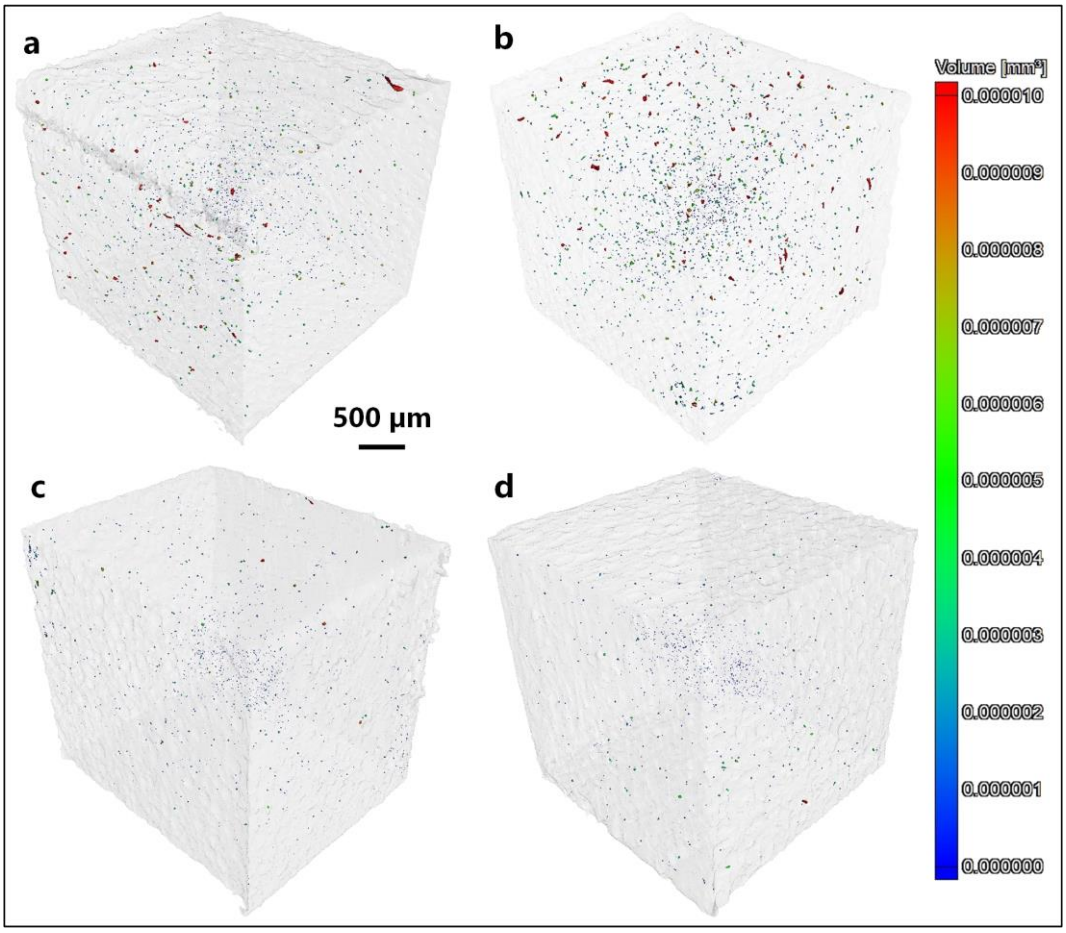

Fig. 5. Reconstructed micro-CT images showing the pore distributions of the (a) as-built; (b) DAT; (c) HIP; and (d) HAT samples.

Fig. 6 shows the defect frequency size distribution in the as-built and heat-treated samples. Based on the micro-CT data shown in Fig. 5, four different ranges of defects were categorised. This result is helpful for further understanding defect elimination efficiency under different conditions. The frequencies for the samples with equivalent

diameters in a range of 5–10 μm showed no obvious differences in the defect number among the four conditions. Approximately 1151 and 1049 defects were detected in the as-built and DAT samples, respectively, while the defect numbers were 1040 and 903 in the HIP and HAT samples, respectively. This result indicates that HIP had only a negligible impact on defects with a very small size. As the defect size exceeded 10 μm, the majority of the defects were closed in both the HIP and HAT samples. There were fewer defects when the defect size was larger. In addition, the frequency of defects larger than 30 m was approximately 19 and 33 for as-built and DAT samples, respectively, whereas no defects were found in HIP and HAT samples. The larger defects were classified as lack of fusion defects, which can be effectively eliminated by HIP.

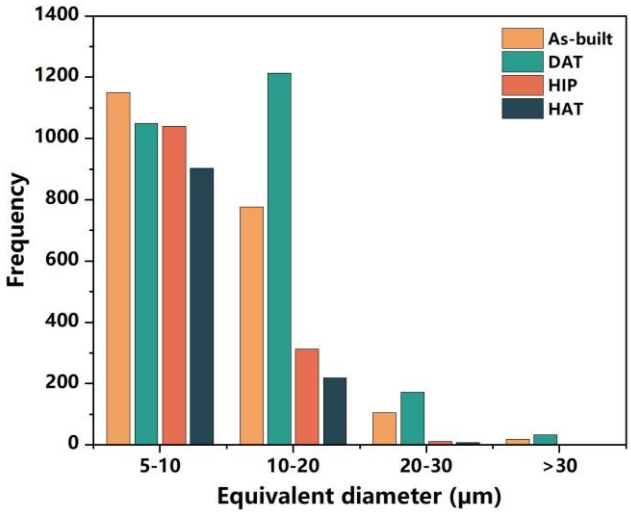

Fig. 6. Defect frequency size distributions in the as-built and heat-treated samples.

3.2 Microstructural observation

Fig. 7 shows the SEM micrographs of the molten pools and the microstructures of the 18Ni-300 maraging steels along the build direction in the as-built and heat-treated conditions. For the as-built sample, the typical molten-pool features and solidification microstructures were observed at different magnifications (Fig. 7a-b). These have been commonly reported in previous studies on LPBF-fabricated alloys [13, 28-30]. The molten pools did not exhibit uniform dimensions (Fig. 7a), possibly due to the 67° rotation that occurred between adjacent layers during processing. High-magnification

images of the microstructure showed the presence of both columnar and cellular structures in the as-built sample (Fig. 7b). Fine cellular structures were formed within the molten pools, whereas the columnar structures grew towards the centre of the molten pool along the build direction. These solidification structures are generally associated with the nature of the LPBF process and have been reported in other studies [13, 20, 21].

The DAT sample showed a similar solidification morphology to that of the as-built sample (Fig. 7c-d). Notably, the LPBF-induced solidification microstructures, including molten pool boundaries, columnar and cellular structures, were still retained. Some studies have reported that molten pools and grain boundaries became vague after ageing [13], but this phenomenon was not observed in this study. By comparison, the structures formed during LPBF disappeared after HIP and were replaced by typical lath-shaped martensite structures with uniform distributions both in the HIP and HAT samples (Fig. 7e-h). These features arose due to grain homogenisation during the HIP process.

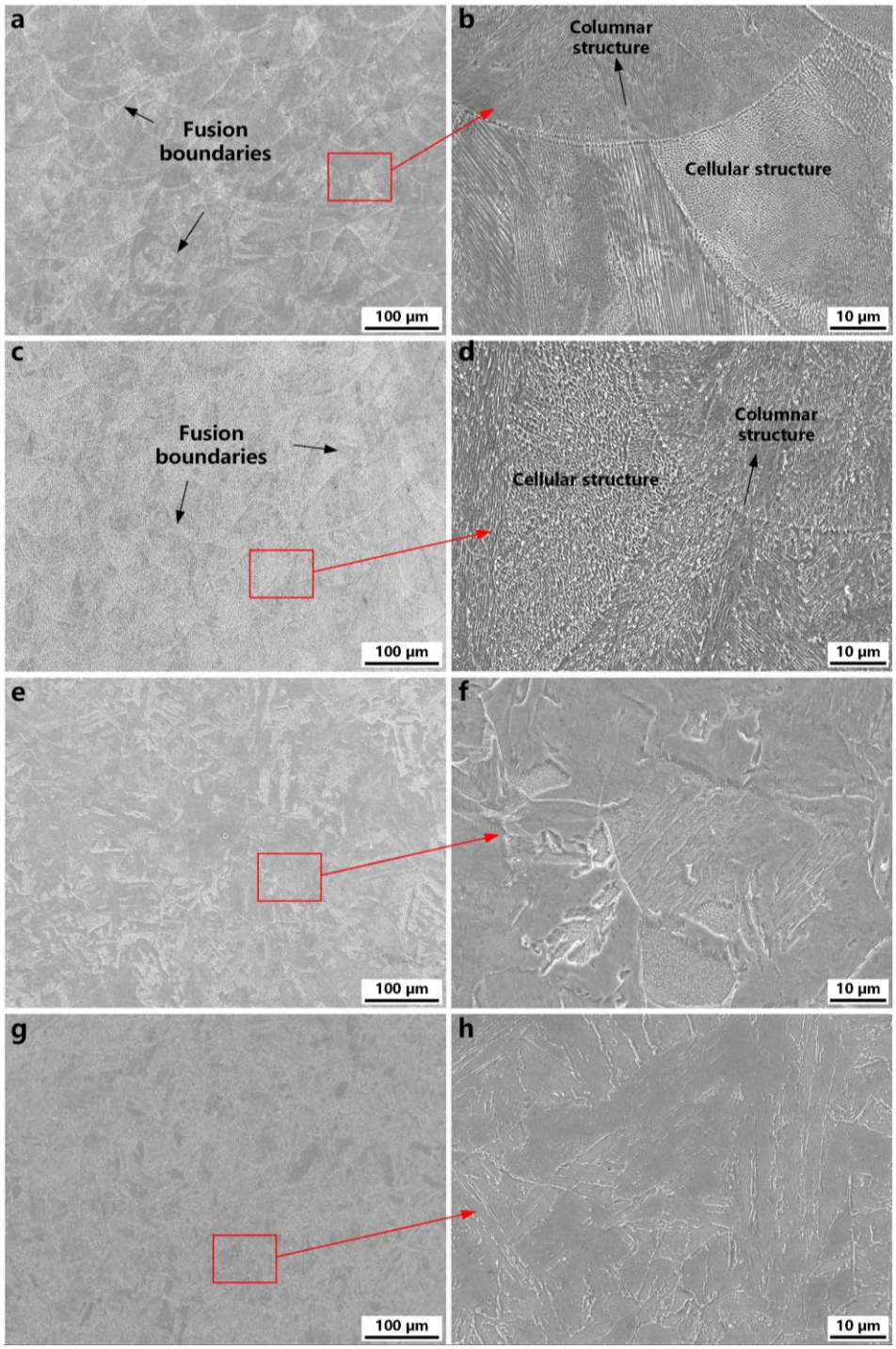

Fig. 7. SEM micrographs showing the molten pool boundaries and solidification microstructures of the samples in the (a-b) as-built; (c-d) DAT; (e-f) HIP; and (g-h) HAT conditions.

Fig. 8 shows the XRD patterns of the as-built and heat-treated 18Ni-300 maraging steel samples. The highest peak intensity was associated with a martensite (α) phase,

which was measured as the major phase in all these conditions. A small percentage of the austenite (γ) phase was also observed; however, the amount of this phase varied slightly in the different heat-treated conditions. The γ phase showed obvious increases after subjecting the as-built sample to DAT, whereas no intensity peaks corresponding to the γ phase were detected and a fully martensitic structure was obtained after subjecting the as-built sample to HIP. A very weak intensity peak of the γ phase was observed in the HAT sample. This result indicated no noticeable reverse transformation of martensite to austenite in the HIP sample during ageing compared to the DAT sample.

The effects of various heat treatments on the phase contents were further evaluated by quantitative measurement of the volume percentage of the γ phase. The content of the retained γ phase in the as-built sample was measured as only 6.22 %, whereas the content of this phase significantly increased to 15.39 % after DAT. This increased γ phase in the aged condition has been defined as reverted austenite in many studies. However, no similar significant increase in reverted austenite after ageing was observed in the HIP samples. Our study findings show that the intensity peaks of the γ phase in the HIP and HAT samples were lower than the detection threshold for identification with the JADE Commercial Software. These results can also support a smaller formation of reverted austenite in the HIP sample during ageing.

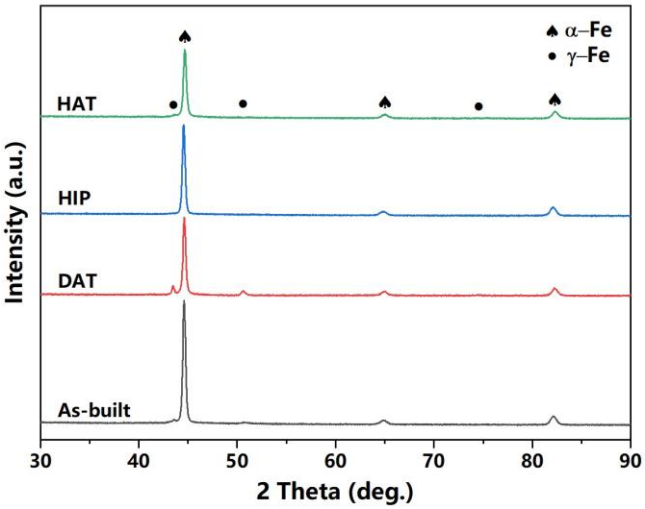

Fig. 8. XRD patterns of the samples in the as-built and heat-treated conditions.

Fig. 9 shows the EBSD inverse pore figure (IPF) mapping micrographs of the as-

built and heat-treated 18Ni-300 maraging steel samples along the build direction. These micrographs are valuable for further exploration of the microstructural differences due to different heat treatment conditions. Fig. 9a-b show that the as-built and DAT samples exhibited a similar grain morphology that was consistent with the microstructure observations shown in Fig. 7. Random grain orientations and massive numbers of small-sized grains were observed in both samples. These were the primary heterogeneous microstructures formed due to the nature of the SLM process, indicating that the ageing condition at 500 ℃ for 6 h employed in this study had no obvious influence on the grain structures.

Compared to these two samples, however, the grain morphology and size differed significantly after the samples were subjected to the HIP process (Fig. 9c-d). These observations show the breakage of the intrinsic grain structures during this process. Noticeably, a homogeneous microstructure morphology was observed, and the grain size became much larger in both samples. Grain growth and high homogenisation of the microstructure were observed in both the HIP and HAT samples, and these two samples also displayed similar microstructure. This observation implied that the HIP process had a significant effect on the grain structures.

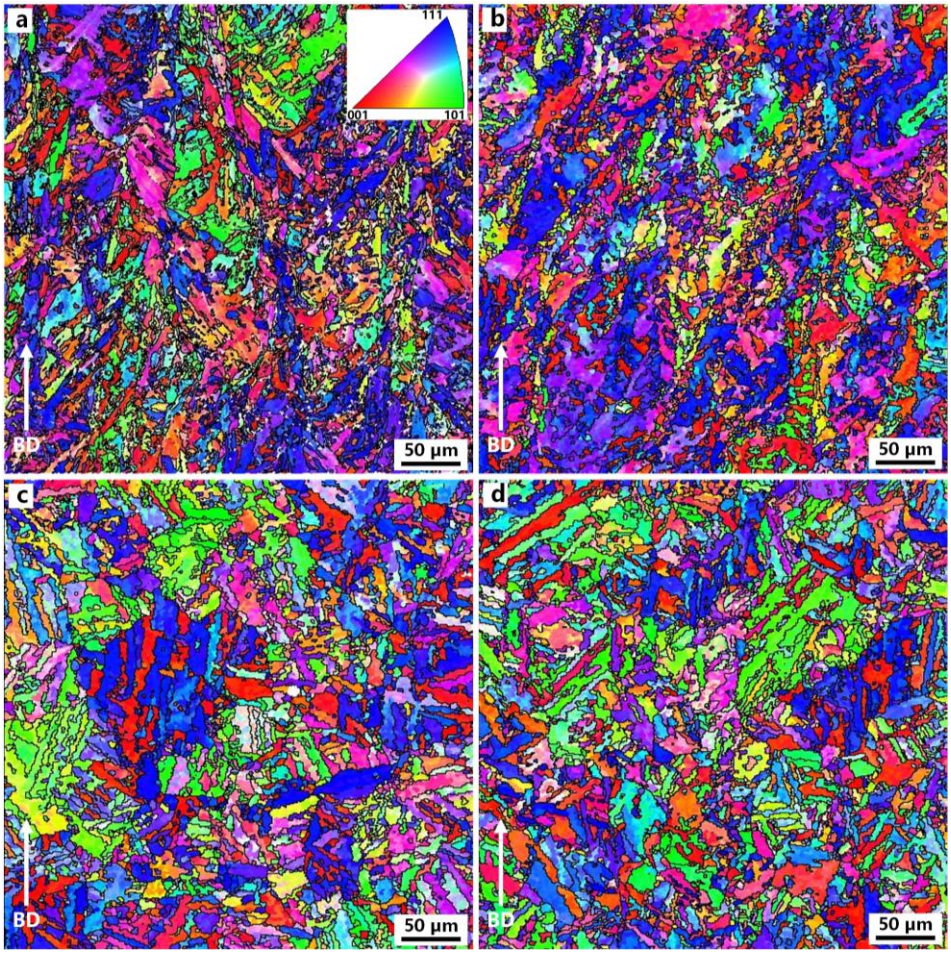

Fig. 9. EBSD inverse pore figure (IPF) mapping micrographs of the samples in (a) as-built; (b) DAT; (c) HIP; and (d) HAT conditions.

The effect of heat treatments on grain shapes was also investigated by calculating the grain aspect ratio (GAR) from the EBSD IPF maps shown in Fig. 9. The as-built, DAT, HIP, and HAT samples contained 3662, 3526, 2690, and 3080 grains, respectively. The significant decrease in the grain number in the HIP-processed conditions suggests that grain growth occurred in both the HIP and HAT samples. The proportion gradually decreased with an increase in the GAR in all the samples, as shown in Figure 10. A GAR value of 1–3 had the highest percentage in all four conditions. The percentages of the GAR in the as-built and DAT samples were calculated as 89.68% and 90.08%, respectively. The high fraction of the GAR value in 1–3 indicates that fine cellular microstructures were formed during LPBF. However, the proportion decreased marginally to 86.27% and 85.26% for the HIP and HAT samples, respectively.

When the GAR value increased to a level higher than 3, a greater grain proportion was observed in the HIP-processed samples. The percentages in the GAR range of 3–6 were 10.27% and 9.81% for the as-built and DAT samples, respectively, while the values increased to 13.00% and 14.12% for the HIP and HAT samples, respectively. In addition, when the GAR value was higher than 6, a very small number of grains were detected after HIP, with fractions of 0.74% and 0.62% for the HIP and HAT samples, respectively. Based on the EBSD results, the average measured diameters of the grains in the as-built and DAT samples were 5.78 ± 3.05 μm and 5.58 ± 3.50 μm, respectively, while the grain size noticeably increased to 7.18 ± 4.79 μm due to the grain growth during HIP at elevated temperature. When the HIP sample was subjected to the aging treatment, the calculated diameter was 6.49 ± 4.11 μm.

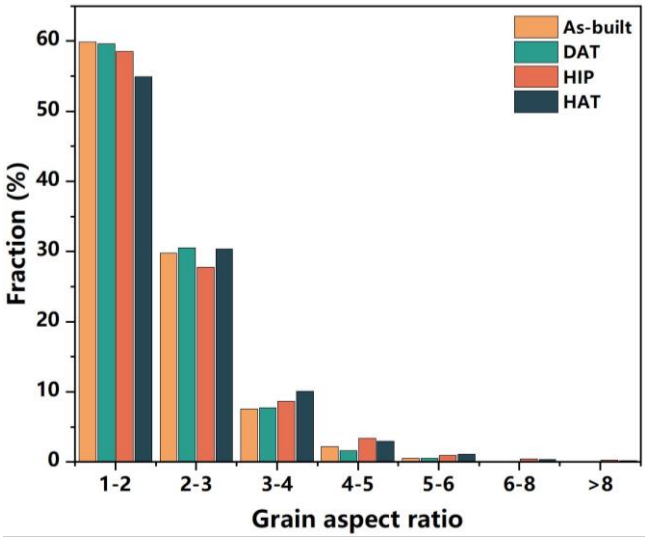

Fig. 10. Grain aspect ratio distribution of the as-built and heat-treated samples.

Fig. 11 shows the grain boundary misorientation angle distributions of the as-built and heat-treated samples corresponding to the EBSD IPF micrographs shown in Fig. 9. with low angle grain boundaries (LAGBs, 2°–15°) and high angle grain boundaries (HAGBs, >15°). The experimental results suggested that the samples produced under the four different conditions contained large amounts of LAGBs. The LAGB fraction in the as-built sample was 52.8% (Fig. 11a), while this fraction significantly increased to 57.2% after DAT (Fig. 11b). However, a slight decrease occurred in the fraction of LAGBs after the HIP process. The HIP and DAT samples contained LAGBs at

percentages with a value of 50.8% and 50.3%, respectively (Fig. 11c-d). Mutua et al. [16] also observed such increase in LAGBs in the DAT sample compared with the as-built sample. The authors explained that this is due to the formation of nanoscale precipitates that impede dislocation movement. The increasing tendency in LAGBs fractions obtained in the as-built and DAT samples was not observed in the HIP and HAT samples.

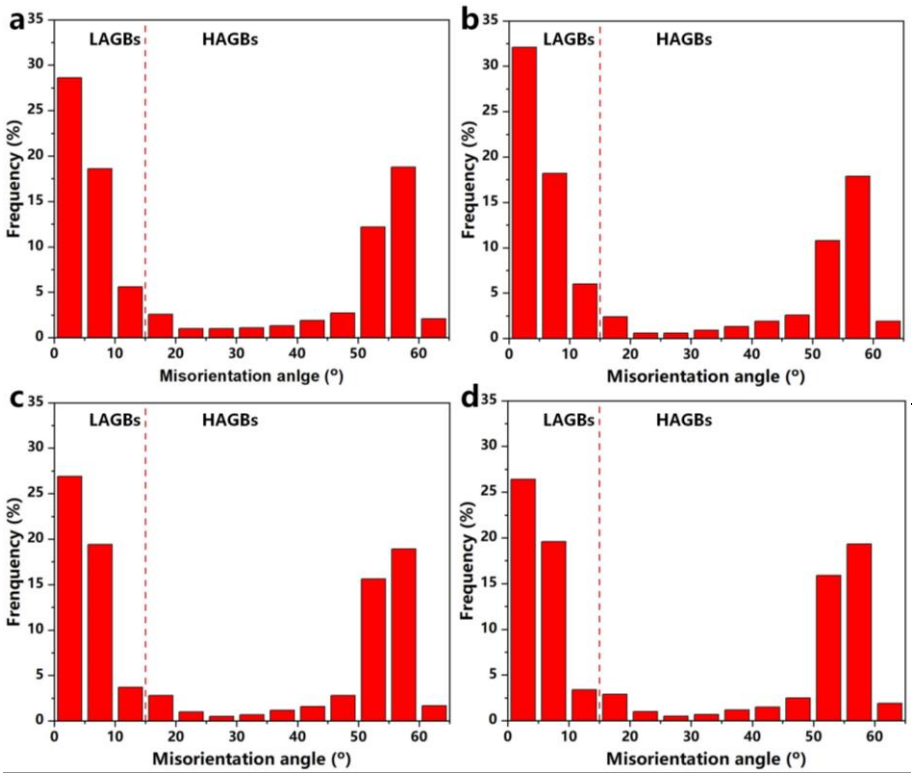

Fig. 11. Grain boundary misorientation angle distributions of the (a) as-built, (b) DAT, (c) HIP and (d) HAT samples.

To further understand the effect of heat treatments on the microstructure and to reveal the strengthening mechanism, TEM observations were performed in the DAT and HAT samples, as shown in Fig. 12. The low-magnification lath martensite microstructures with high dislocation density were primarily observed in the matrix of both samples in bright-field (BF) TEM micrographs at low magnification (Fig. 12a and d). Fig. 12b-c and e-f show the high-magnification BF-TEM micrographs and the corresponding selected area electron diffraction (SAED) patterns. Massive nanoscale precipitations were observed in the BF-TEM micrographs in the matrix of both the DAT

and HAT samples (Fig. 12b and e). These precipitations can improve strength. Fig. 12g and h, which show the dark field TEM micrographs of the DAT and HAT samples, respectively, reveal the formation of massive precipitates with a highly uniform distribution in both samples. However, the size of the nanoscale precipitates was larger in the HAT sample than in the DAT sample. Previous studies have confirmed an association of these nanoscale precipitates with the formation of Ni_3Ti and Ni_3Mo in the matrix [17, 20]. Jägle et al. [7] reported that the nanoscale precipitates can be mainly divided into two types based on their shapes and sizes. The spherical shape precipitates could be Ni_3Mo, while the needle shape precipitates could be Ni_3Ti. These two types of precipitates were not simultaneously formed during ageing treatment. As Tan et al. reported, because of the faster precipitation kinetics of Ti, Ni_3Ti nanoscale precipitates generally form quickly during ageing treatment, and then these precipitates can act as a nucleation site for the formation of Ni_3Mo precipitates [17].

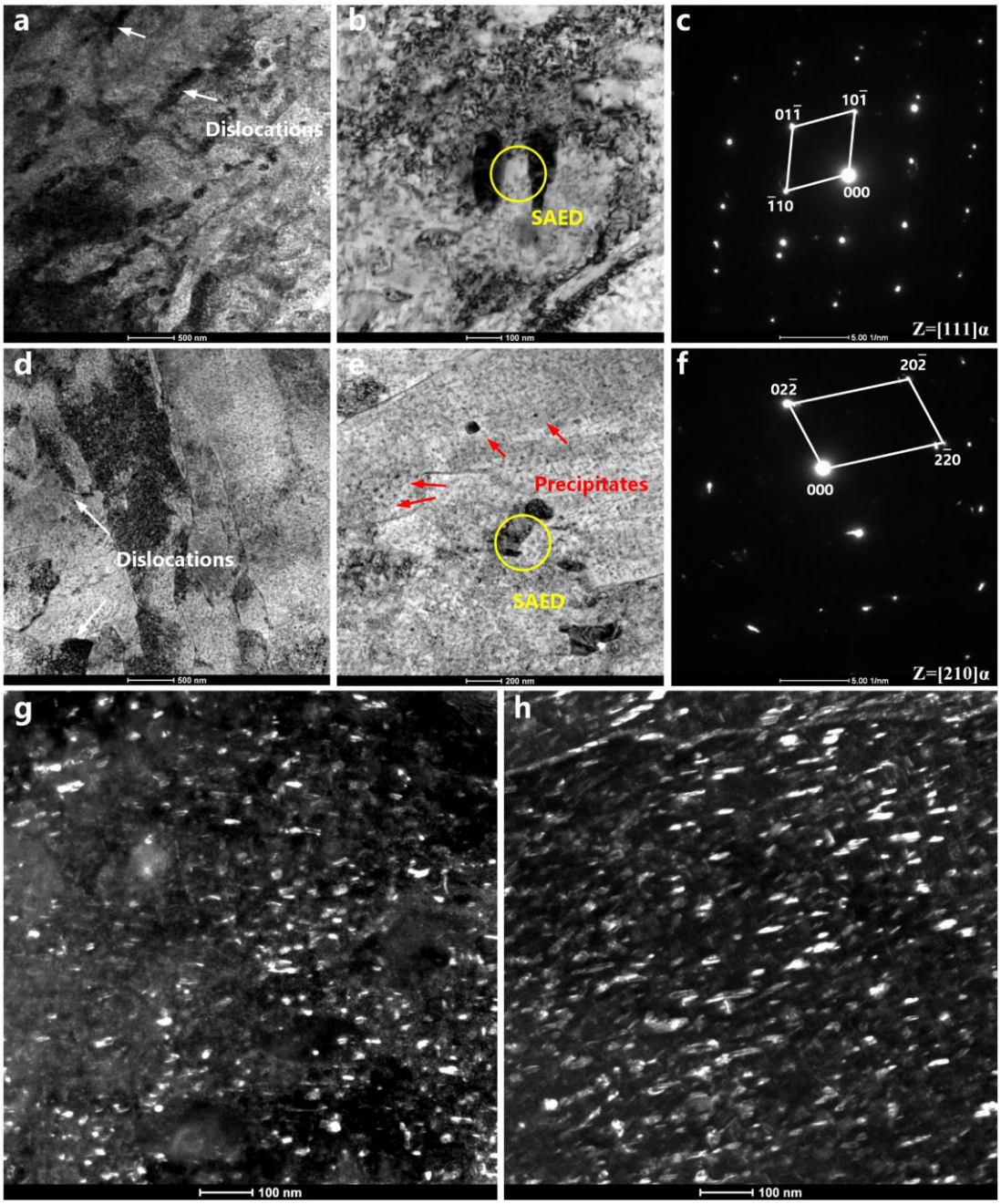

Fig. 12. Bright-field (BF) TEM micrographs and corresponding SAED patterns of the DAT and HAT samples: (a) BF micrograph and (b-c) corresponding SAED patterns of the DAT sample; (d) BF micrograph and (e-f) corresponding SAED patterns of the HAT sample; and (g-h) dark-field TEM micrographs showing the nanoscale precipitates of the DAT and HAT samples, respectively.

3.3 Mechanical behaviours

Fig. 13 shows the tensile properties of the 18Ni-300 maraging steel material in the as-built and heat-treated conditions following uniaxial tensile testing. The detailed

tensile performances are summarised in Fig. 13b. The tensile performances were consistent for the samples in each condition. The as-built samples had a 1081 ± 16 MPa yield strength (YS), 1184 ± 5 MPa ultimate tensile strength (UTS), and 15.4 ± 1% elongation to failure. By contrast, after HIP treatment, the YS and UTS dropped dramatically to 725 ± 28 MPa and 972 ± 2 MPa, respectively, while elongation to failure showed only a small change (14.3 ± 0.2%) compared with the as-built samples. In general, the ductility behaviour of LPBF-built parts, such as 316L stainless steel [23] and nickel-based alloys [31], was enhanced by HIP treatment. Although most pores can be eliminated and residual stress can be released by HIP treatment, this expected enhanced ductility behaviour was not observed in our study. Han et al. [21] also obtained similar results in their study on the tensile performance of as-built and HIP Hastelloy X alloys. Those studies showed a similar result, indicating that residual gas pores were not closed during HIP.

Compared with the as-built and HIP samples, the DAT and HAT samples showed a significant increase in tensile strength. The DAT samples had the maximum YS and UTS values of 1751 ± 24 MPa and 1780 ± 14 MPa, respectively, together with an elongation of 3.2 ± 0.6%. The HIP/ageing treatment resulted in a simultaneous enhancement of strength and ductility compared to the DAT samples. The HAT samples resulted in values for YS, UTS and elongation to failure of 1796 ± 4 MPa, 1885 ± 3 MPa and 6.3 ± 0.6%, respectively. This behaviour contrasted with the reduction in strength observed with the conventional solution-ageing treatment combination [17]. The YS and UTS were approximately 50 MPa and 105 MPa higher, respectively, for the HAT samples than for the DAT samples, while the elongation to failure increased by almost 100% in the HAT samples. This result indicated a concurrent enhancement of strength and ductility compared to the DAT samples.

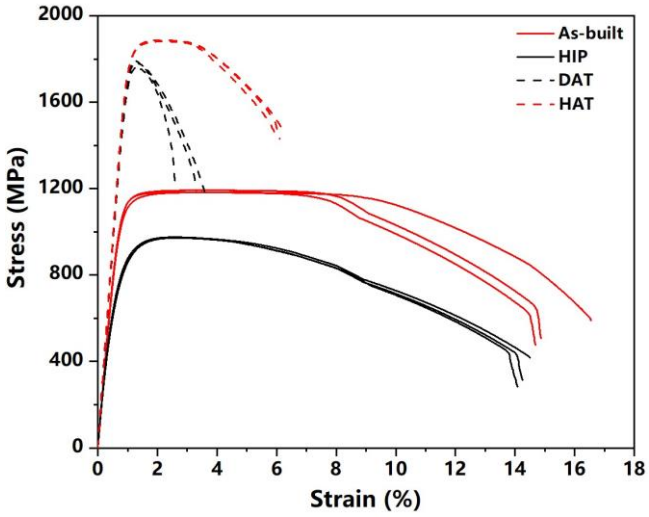

Fig. 13. Uniaxial tensile stress-strain curves of the as-built and heat-treated 18Ni-300 maraging steel samples.

Table 1. Mechanical properties from tensile tests of the as-fabricated and heat-treated samples.

Samples	Yield strength (MPa)	Ultimate tensile strength (MPa)	Elongation (%)
As-built	1081±16	1184±5	15.4±1
HIP	725±28	972±2	14.3±0.2
DAT	1751±24	1780±14	3.2±0.6
HAT	1796±4	1885±3	6.3±0.6

Fig. 14 shows different magnifications of the fracture surface morphology of the 18Ni-300 maraging steel samples in the as-built and HAT conditions following tensile tests. Since the HIP and DAT samples exhibited similar fracture surfaces compared to the as-built and HAT samples, respectively, the fracture morphology of these two samples is not shown. The low-magnification observation of the fracture surfaces revealed a clear necking in the as-built samples (Fig. 14a). The presence of the necking behaviour was associated with the higher elongation results in the as-built and HIP samples. The high-magnification images show the presence of a great number of fine dimples (Fig. 14b-c). Therefore, the fracture mechanism for the as-built samples was a ductile mode. However, the low-magnification micrographs of the HAT samples showed a flat fracture surface and indistinct necking (Fig. 14d). At high magnification,

shallow dimples were only observed in limited areas in the fracture surfaces. Several cleavage-like fractures were also detected in the fracture surface, indicating a brittle transgranular fracture. Hence, both results suggested that the fracture mechanism changed from a ductile pattern in the as-built condition to a combined ductile and brittle pattern in the HAT conditions.

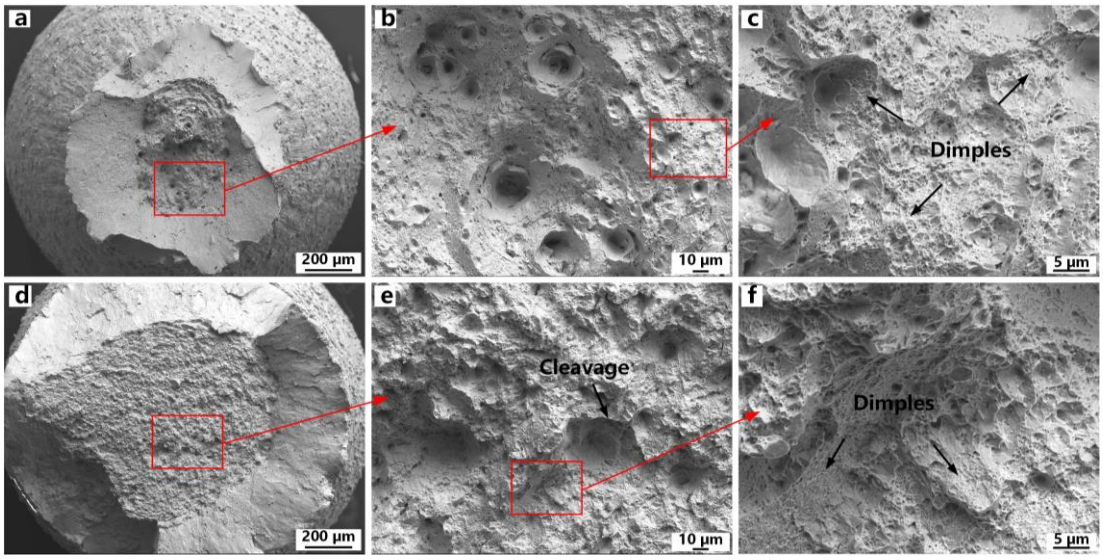

Fig. 14. SEM micrographs showing the fracture surfaces of the (a-c) as-built and (d-f) HAT samples at different magnifications.

Fig. 15 shows the room-temperature Vickers microhardness of the as-built and post-treated samples of 18Ni-300 maraging steel. These results were consistent with the tensile strength results. The as-built samples had an average hardness value of 361±7 HV, but the samples exhibited a severe decrease in hardness after the HIP treatment. The measured average hardness was roughly 13% lower for the HIP sample (314±6 HV) than for the as-built sample. By contrast, a significant increase in hardness (595±14 HV) was achieved in samples subjected to ageing treatments, as the hardness was approximately 65% higher in those samples than in the as-built sample. The measured hardness value of the sample subjected to combined heat treatments was further increased to 623±10 HV.

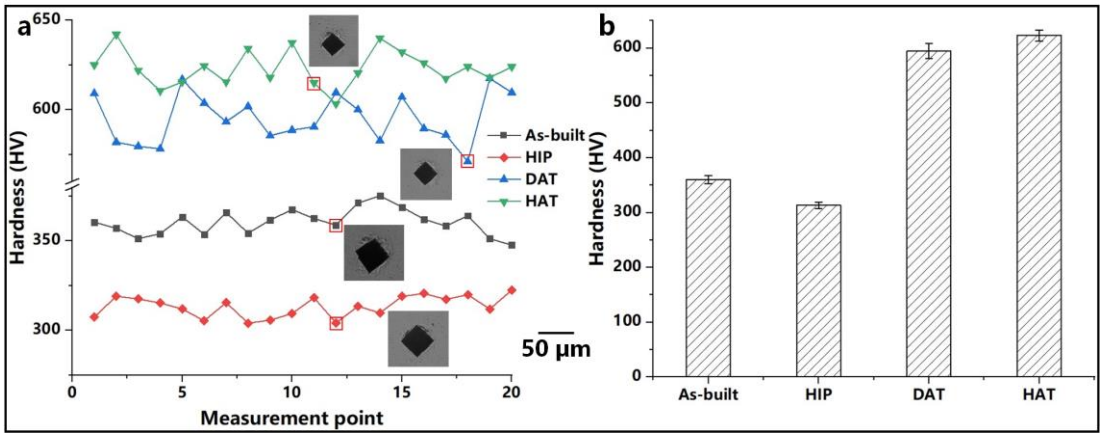

Fig. 15. The Vickers microhardness measurements of the samples at different conditions.

4. Discussion

4.1 Effect of heat treatments on densification and microstructure

In general, LPBF-fabricated samples have almost full densification when employing the optimal process parameters. As illustrated in Figs. 3-5, the density measurements and defect observations in this study are consistent with this principle; however, several defects, such as microcracks and gas pores, and lack of fusions, are inevitable in the samples even under the optimal manufacturing condition [6, 27]. These defects cannot be effectively eliminated by adjusting the process parameters. Therefore, the HIP process has been widely employed for LPBF-fabricated materials due to the high efficiency of pore closure [21, 32-34]. The experimental results shown in Fig. 4 and 5 demonstrated that the primary defects of LPBF-fabricated 18Ni-300 maraging steels under the optimal process condition were gas pores and lack of fusion defects, but most defects formed in the as-fabricated condition can be successfully eliminated after HIP (Figs. 4c and 5c). Defect annihilation takes place during HIP operation due to various mechanisms such as diffusional flow of vacancies or strong local plastic deformation by dislocation slip around the defects [35].

Note that the present study only considered the internal pores in the middle areas of the samples. Some studies have demonstrated that some pores near the surfaces remain after HIP [36-38], but this was not the focus of the present research. The residual

pores that remained after HIP were classified as argon gas pores, which cannot be closed by this process. In addition, both OM and micro-CT observations shown in Figs. 4c-d and 5c-d indicated that large-sized defects, such as those formed by lack of fusions, were only observed near the surface in the HIP and HAT samples. This is because that the confining gas can penetrate into these defects during HIP [37]. This result confirmed that the subsequent ageing treatment had little effect on the pores of the HIP sample. Further research is required to study the effect of various subsequent ageing conditions on the defect closure efficiency of the HIP samples.

The XRD results shown in Fig. 8 indicate that a complete transformation of austenite to martensite phase could be obtained for the as-built 18Ni-300 maraging steels after the HIP process. The temperature of the HIP treatment at 1050 °C employed in this study was above the finish temperature of martensite to austenite (about 750 °C). This indicated that a full austenisation state could be obtained after a fairly short holding time of 3 h during HIP, and then the complete martensite phase was transformed upon the cooling stage. As Tan et al. [17] and Conde et al. [39] reported in LPBF-fabricated 18Ni-300 maraging steel, complete martensitic structures can be obtained with an extremely slow cooling rate during the transformation from the austenite to the martensite phase. In addition, the reverted austenite was easier to form in the as-built condition than in the HIP condition during ageing. This is due to the formation of LPBF-induced heterogeneous microstructures, which could contribute to further austenite reversion by nucleation at segregations or growth at the retained austenite areas [39]. However, as the EBSD results in Fig. 9 show, HIP resulted in greater grain growth and homogenisation than was observed in the DAT condition. This could reduce the nucleation sites, thereby preventing the austenite reversion during ageing. The above analysis showed that HIP had a similar effect on the microstructure to that seen with the traditional solution treatment that is extensively reported in the literature.

4.2 Analysis of strengthening mechanisms

The microstructure development of the LPBF-fabricated 18Ni-300 maraging steel

subjected to different heat treatments is shown in Fig. 16. The experimental results demonstrated that the tensile strength and microhardness of LPBF-manufactured18Ni-300 maraging steels decreased after HIP and significantly improved after ageing compared to the as-built condition. Combined HIP and ageing heat treatment simultaneously improved the strength as well as the ductility compared with the direct aged treatment. Based on the tensile strength analysis (Fig. 13 and Table 1), the combination of HIP and ageing contributed to an approximately 50 MPa increase in yield strength and a 100 MPa increase in ultimate tensile strength compared to the direct ageing treatment. This observation differs from the strength-ductility trade-off through the traditional solution and ageing heat treatments studied in the literature [12, 17]. This improvement in tensile strength was attributed to the massive nanoscale precipitates formed during ageing compared to the as-built and HIP samples. The primary strengthening mechanism for this great improvement of tensile strength and microhardness arose by the formation of these precipitates, which is known as the Orowan strengthening mechanism that can be expressed as [17, 20]:

$$\begin{cases} \sigma_A = \sigma_0 + \dfrac{Gb}{2\pi k(\alpha - d)} ln \dfrac{(\alpha - d)}{2b} \\ \dfrac{1}{k} = \dfrac{1}{2}\left(\dfrac{1}{1-\varepsilon} + 1\right) \end{cases}$$

Where σ_0 and G are the yield strength and shear modulus of the matrix, respectively, b is the Bergers vector, α is the interspace of nanoscale precipitates, d is the equivalent diameter of the precipitates, and ε is the Poisson's ratio. G is about 71 GPa, ε is 0.3, and $\boldsymbol{b}$ for maraging steel is approximately 0.249 nm [17]. Based on the TEM analysis (Fig. 12g and h), the interspaces of the nanoscale precipitates were measured as 28.2 nm and 23.5 nm for the DAT and HAT samples, respectively, while the equivalent diameters were calculated as 10.8 nm and 14.8 nm for the DAT and HAT samples, respectively. Therefore, the quantitatively calculated enhancement of the strength induced by the formation of nanoscale precipitates in the DAT and HAT samples were approximately 692 MPa and 1119 MPa, respectively. This difference could be due to the difference in the availability of Ni in the matrix between the as-built

and HIP samples. The XRD and EBSD results showed that the sufficient homogenisation and a lower fraction of reverted austenite phase, when subjected to the HIP at 1050 ℃, were observed in the HIP samples compared to the as-built sample, as illustrated in Figs. 8 and 9. This could result in higher availability of Ni in the matrix in the HIP samples and benefit the formation of more nanoscale precipitates during ageing [39]. Therefore, the difference in strength was observed between DAT and HAT samples.

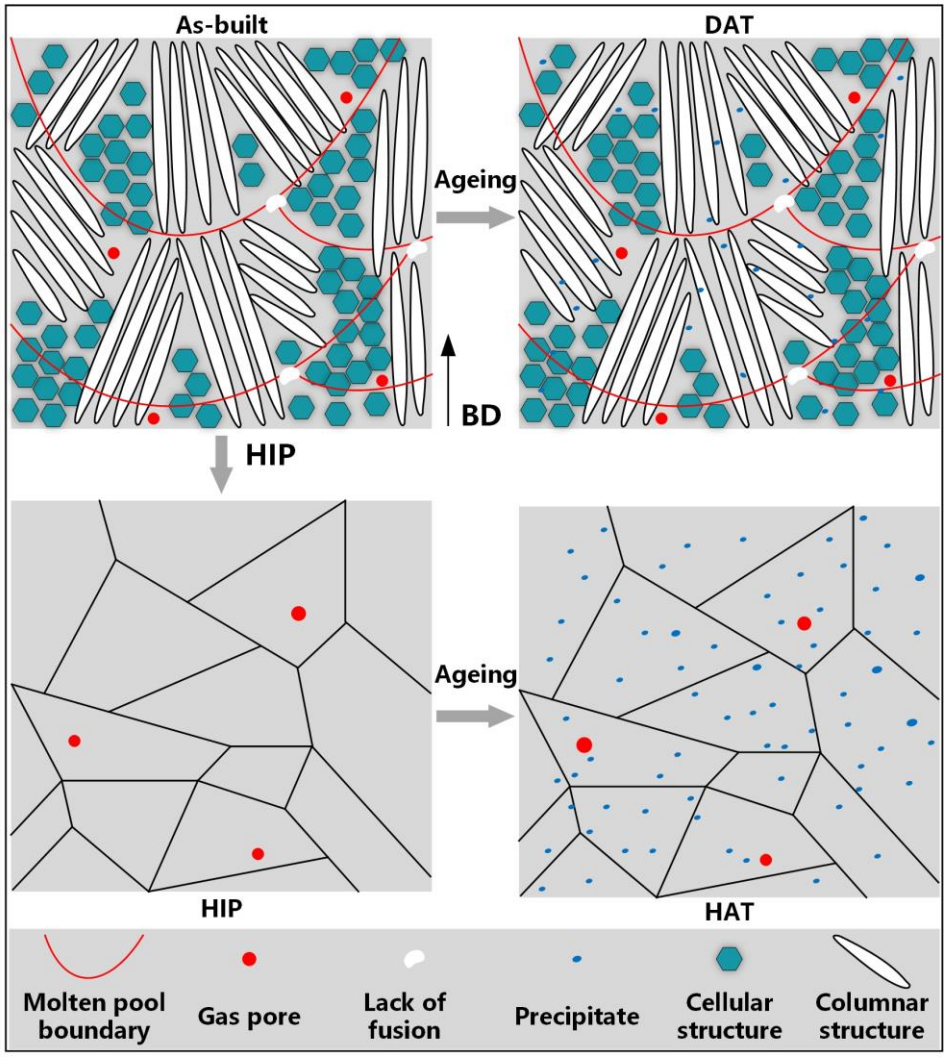

Fig. 16. Schematic diagram showing the microstructure development of the LPBF-fabricated 18Ni-30 maraging steel subjected to different heat treatments.

As shown in Table. 1, the ductility value increased from 3.2 ± 0.6 % under DAT to 6.3 ± 0.6 % under HAT, demonstrating that HIP before ageing can contribute to

almost twice the elongation. This obvious improvement can be explained by two factors. One was that the HIP process eliminated the number of embedded pores formed during LPBF. The other was that grain growth and a high degree of recrystallisation occurred during HIP at 1050 ℃ for 3 h. Therefore, this process promoted the elimination of the retained residual stress in the samples formed during LPBF and decreased the dislocation density [24, 40]. Both also contributed to the improvement of the elongation. The fraction of the austenite phase was higher in the DAT samples than in the HAT sample. This increased reverse transformation of martensite to austenite during ageing deteriorated the strength but contributed to the improvement of ductility reported in some earlier literature [39]; however, the content of approximately 15.39 % of reverted austenite was still very low in the DAT samples. Therefore, the pore closure and grain growth after HIP might play a more critical role in improving the elongation to failure during room-temperature tensile testing.

5. Conclusions

This study applied the HIP process on 18Ni-300 maraging steels fabricated by LPBF and comprehensively investigated the effect of direct ageing and combined HIP+ageing treatments on the microstructure and mechanical behaviours. The following main conclusions are drawn:

(1) Hot isostatic pressing was employed for 18Ni-300 maraging steel fabricated by LPBF. The experimental result demonstrated that the HIP process can substantially improve the relative density, increasing from 99.6% in the as-built condition to 99.96%. Both optical and micro-CT observations confirmed that only a small number of residual gas pores remained that cannot be closed by this process. In addition, the study showed that subsequent ageing treatment on the HIP samples had no significant effect on the defect reopening.

(2) The HIP process resulted in the disappearance of the typical LPBF-induced heterogeneous microstructure and replacement by full lath martensitic structures. In addition, the susceptibility to the formation of reverted transformation of martensite to austenite was less in the HIP sample than in the as-built sample

during ageing. In addition, the TEM investigations detected the formation of massive nanoscale precipitates in both DAT and HAT samples. This was associated with Ni_3Ti and Ni_3Mo nanoscale precipitates formed during ageing; however, the HAT sample had a higher size and density.

(3) Compared to the as-built samples, a great improvement was achieved in yield strength, ultimate tensile strength and microhardness after DAT. In addition, the HIP process before ageing can contribute to simultaneous upgrade enhancement of strength and elongation compared to DAT. The results show that the room-temperature ultimate tensile strength and elongation to failure after HAT were approximately 6% and 100% higher than those after DAT, respectively. As a result of the differences in nanoscale precipitates, the DAT and HAT samples had quantitative strength enhancements of 692 MPa and 1119 MPa, respectively.

These findings suggested that LPBF-fabricated 18Ni-300 maraging steels with simultaneous improvement of strength and ductility can be obtained using a combination of HIP and ageing heat treatments. However, the present study considered only one ageing condition. It is well-known that the ageing treatment plays a critical role in the formation of nanoscale precipitates and mechanical properties. Therefore, future work will concentrate on studying the effect of other ageing conditions, in combination with HIP, on the microstructure and mechanical behaviours of 18Ni-300 maraging steel fabricated by LPBF. The aim is to explore the possibility of achieving higher strength and ductility combinations by optimising the ageing in different temperatures and holding times.

Data availability

The raw/processed data required to reproduce these findings cannot be shared at this time as the data also forms part of an ongoing study.

Acknowledgements

This paper was financially supported by the National Natural Science Foundation of China (Grant No: 51975073, 51805052). The lead author (Jun Song) gratefully

acknowledges the financial support from China Scholarship Council (CSC).

References

[1] D. Gu, X. Shi, R. Poprawe, D.L. Bourell, R. Setchi, J. Zhu, Material-structure-performance integrated laser-metal additive manufacturing, Science. 372 (2021). https://doi.org/10.1126/science.abg1487.

[2] Q. Feng, Q. Tang, Y. Liu, R. Setchi, S. Soe, S. Ma, L. Bai, Quasi-static analysis of mechanical properties of Ti6Al4V lattice structures manufactured using selective laser melting, Int. J. Adv. Manuf. Technol. 94 (2018) 2301–2313. https://doi.org/10.1007/s00170-017-0932-7.

[3] Y. Liu, H. Xu, L. Zhu, X. Wang, Q. Han, S. Li, Y. Wang, R. Setchi, D. Wang, Investigation into the microstructure and dynamic compressive properties of selective laser melted Ti–6Al–4V alloy with different heating treatments, Mater. Sci. Eng. A. 805 (2021) 140561. https://doi.org/10.1016/j.msea.2020.140561.

[4] J. Song, Q. Tang, Q. Feng, Q. Han, S. Ma, H. Chen, F. Guo, R. Setchi, Effect of remelting processes on the microstructure and mechanical behaviours of 18Ni-300 maraging steel manufactured by selective laser melting, Mater. Charact. 184 (2022) 111648. https://doi.org/10.1016/j.matchar.2021.111648.

[5] N.T. Aboulkhair, N.M. Everitt, I. Ashcroft, C. Tuck, Reducing porosity in AlSi10Mg parts processed by selective laser melting, Addit. Manuf. 1 (2014) 77–86. https://doi.org/10.1016/j.addma.2014.08.001.

[6] Q. Han, Y. Gu, R. Setchi, F. Lacan, R. Johnston, S.L. Evans, S. Yang, Additive manufacturing of high-strength crack-free Ni-based Hastelloy X superalloy, Addit. Manuf. 30 (2019) 100919. https://doi.org/10.1016/j.addma.2019.100919.

[7] E.A. Jägle, P.P. Choi, J. Van Humbeeck, D. Raabe, Precipitation and austenite reversion behavior of a maraging steel produced by selective laser melting, J. Mater. Res. 29 (2014) 2072–2079. https://doi.org/10.1557/jmr.2014.204.

[8] G. Casalino, S.L. Campanelli, N. Contuzzi, A.D. Ludovico, Experimental investigation and statistical optimisation of the selective laser melting process of a maraging steel, Opt. Laser Technol. 65 (2015) 151–158. https://doi.org/10.1016/j.optlastec.2014.07.021.

[9] A.F. de Souza, K.S. Al-Rubaie, S. Marques, B. Zluhan, E.C. Santos, Effect of laser speed, layer thickness, and part position on the mechanical properties of maraging 300 parts manufactured by selective laser melting, Mater. Sci. Eng. A. 767 (2019) 138425. https://doi.org/10.1016/j.msea.2019.138425.

[10] Y. Bai, C. Zhao, D. Wang, H. Wang, Evolution mechanism of surface morphology and internal hole defect of 18Ni300 maraging steel fabricated by selective laser melting, J. Mater. Process. Technol. 299 (2022) 117328. https://doi.org/10.1016/j.jmatprotec.2021.117328.

[11] Y. Bai, D. Wang, Y. Yang, H. Wang, Effect of heat treatment on the microstructure and mechanical properties of maraging steel by selective laser melting, Mater. Sci. Eng. A. 760 (2019) 105–117. https://doi.org/10.1016/j.msea.2019.05.115.

[12] J. Song, Q. Tang, Q. Feng, S. Ma, R. Setchi, Y. Liu, Q. Han, X. Fan, M. Zhang, Effect of heat treatment on microstructure and mechanical behaviours of 18Ni-300 maraging steel manufactured by selective laser melting, Opt. Laser Technol. 120 (2019) 105725. https://doi.org/10.1016/j.optlastec.2019.105725.

[13] T. Allam, K.G. Pradeep, P. Köhnen, A. Marshal, J.H. Schleifenbaum, C. Haase, Tailoring the nanostructure of laser powder bed fusion additively manufactured maraging steel, Addit. Manuf. 36 (2020). https://doi.org/10.1016/j.addma.2020.101561.

[14] E.A. Jägle, Z. Sheng, P. Kürnsteiner, S. Ocylok, A. Weisheit, D. Raabe, Comparison of maraging steel micro- and nanostructure produced conventionally and by laser additive manufacturing, Materials (Basel). 10 (2017). https://doi.org/10.3390/ma10010008.

[15] K. Kempen, E. Yasa, L. Thijs, J.P. Kruth, J. Van Humbeeck, Microstructure and mechanical properties of selective laser melted 18Ni-300 steel, Phys. Procedia. 12 (2011) 255–263. https://doi.org/10.1016/j.phpro.2011.03.033.

[16] J. Mutua, S. Nakata, T. Onda, Z.C. Chen, Optimization of selective laser melting parameters and influence of post heat treatment on microstructure and mechanical properties of maraging steel, Mater. Des. 139 (2018) 486–497. https://doi.org/10.1016/j.matdes.2017.11.042.

[17] C. Tan, K. Zhou, W. Ma, P. Zhang, M. Liu, T. Kuang, Microstructural evolution, nanoprecipitation behavior and mechanical properties of selective laser melted high-performance grade 300 maraging steel, Mater. Des. 134 (2017) 23–34. https://doi.org/10.1016/j.matdes.2017.08.026.

[18] R. Casati, J.N. Lemke, A. Tuissi, M. Vedani, Aging behaviour and mechanical performance of 18-Ni 300 steel processed by selective laser melting, Metals (Basel). 6 (2016) 218. https://doi.org/10.3390/met6090218.

[19] S. Yin, C. Chen, X. Yan, X. Feng, R. Jenkins, P. O'Reilly, M. Liu, H. Li, R. Lupoi, The influence of aging temperature and aging time on the mechanical and tribological properties of selective laser melted maraging 18Ni-300 steel, Addit. Manuf. 22 (2018) 592–600. https://doi.org/10.1016/j.addma.2018.06.005.

[20] S. Dehgahi, M. Sanjari, M.H. Ghoncheh, B.S. Amirkhiz, M. Mohammadi, Concurrent improvement of strength and ductility in heat-treated C300 maraging steels produced by laser powder bed fusion technique, Addit. Manuf. 39 (2021) 101847. https://doi.org/10.1016/j.addma.2021.101847.

[21] Q. Han, R. Mertens, M.L. Montero-Sistiaga, S. Yang, R. Setchi, K. Vanmeensel, B. Van Hooreweder, S.L. Evans, H. Fan, Laser powder bed fusion of Hastelloy X: Effects of hot isostatic pressing and the hot cracking mechanism, Mater. Sci. Eng. A. 732 (2018) 228–239. https://doi.org/10.1016/j.msea.2018.07.008.

[22] W. Tillmann, C. Schaak, J. Nellesen, M. Schaper, M.E. Aydinöz, K.P. Hoyer, Hot isostatic pressing of IN718 components manufactured by selective laser melting, Addit. Manuf. 13 (2017) 93–102. https://doi.org/10.1016/j.addma.2016.11.006.

[23] N.P. Lavery, J. Cherry, S. Mehmood, H. Davies, B. Girling, E. Sackett, S.G.R. Brown, J. Sienz, Effects of hot isostatic pressing on the elastic modulus and

tensile properties of 316L parts made by powder bed laser fusion, Mater. Sci. Eng. A. 693 (2017) 186–213. https://doi.org/10.1016/j.msea.2017.03.100.
[24] S. Sun, Q. Teng, Y. Xie, T. Liu, R. Ma, J. Bai, C. Cai, Q. Wei, Two-step heat treatment for laser powder bed fusion of a nickel-based superalloy with simultaneously enhanced tensile strength and ductility, Addit. Manuf. 46 (2021) 102168. https://doi.org/10.1016/j.addma.2021.102168.
[25] Z. Mao, X. Lu, H. Yang, X. Niu, L. Zhang, X. Xie, Processing optimization, microstructure, mechanical properties and nanoprecipitation behavior of 18Ni300 maraging steel in selective laser melting, Mater. Sci. Eng. A. 830 (2022) 142334. https://doi.org/10.1016/j.msea.2021.142334.
[26] C.Y. Wang, J. Shi, W.Q. Cao, H. Dong, Characterization of microstructure obtained by quenching and partitioning process in low alloy martensitic steel, Mater. Sci. Eng. A. 527 (2010) 3442–3449. https://doi.org/10.1016/j.msea.2010.02.020.
[27] C. Cai, C. Radoslaw, J. Zhang, Q. Yan, S. Wen, B. Song, Y. Shi, In-situ preparation and formation of TiB/Ti-6Al-4V nanocomposite via laser additive manufacturing: Microstructure evolution and tribological behavior, Powder Technol. 342 (2019) 73–84. https://doi.org/10.1016/j.powtec.2018.09.088.
[28] Y. Bai, C. Zhao, J. Zhang, H. Wang, Abnormal thermal expansion behaviour and phase transition of laser powder bed fusion maraging steel with different thermal histories during continuous heating, Addit. Manuf. 53 (2022) 102712. https://doi.org/10.1016/j.addma.2022.102712.
[29] D. Tomus, Y. Tian, P.A. Rometsch, M. Heilmaier, X. Wu, Influence of post heat treatments on anisotropy of mechanical behaviour and microstructure of Hastelloy-X parts produced by selective laser melting, Mater. Sci. Eng. A. 667 (2016) 42–53. https://doi.org/10.1016/j.msea.2016.04.086.
[30] S. Dehgahi, M.H. Ghoncheh, A. Hadadzadeh, M. Sanjari, B.S. Amirkhiz, M. Mohammadi, The role of titanium on the microstructure and mechanical properties of additively manufactured C300 maraging steels, Mater. Des. 194 (2020) 108965. https://doi.org/10.1016/j.matdes.2020.108965.
[31] F.A. Baskov, Z.A. Sentyurina, Y.Y. Kaplanskii, I.A. Logachev, A.S. Semerich, E.A. Levashov, The influence of post heat treatments on the evolution of microstructure and mechanical properties of EP741NP nickel alloy produced by laser powder bed fusion, Mater. Sci. Eng. A. 817 (2021) 141340. https://doi.org/10.1016/j.msea.2021.141340.
[32] J. Kunz, A. Boontanom, S. Herzog, P. Suwanpinij, A. Kaletsch, C. Broeckmann, Influence of hot isostatic pressing post-treatment on the microstructure and mechanical behavior of standard and super duplex stainless steel produced by laser powder bed fusion, Mater. Sci. Eng. A. 794 (2020) 139806. https://doi.org/10.1016/j.msea.2020.139806.
[33] Y.Y. Kaplanskii, E.A. Levashov, A. V. Korotitskiy, P.A. Loginov, Z.A. Sentyurina, A.B. Mazalov, Influence of aging and HIP treatment on the structure and properties of NiAl-based turbine blades manufactured by laser powder bed fusion, Addit. Manuf. 31 (2020) 100999.

https://doi.org/10.1016/j.addma.2019.100999.
[34] X. Yan, S. Yin, C. Chen, C. Huang, R. Bolot, R. Lupoi, M. Kuang, W. Ma, C. Coddet, H. Liao, M. Liu, Effect of heat treatment on the phase transformation and mechanical properties of Ti6Al4V fabricated by selective laser melting, J. Alloys Compd. 764 (2018) 1056–1071. https://doi.org/10.1016/j.jallcom.2018.06.076.
[35] A. Epishin, B. Fedelich, T. Link, T. Feldmann, I.L. Svetlov, Pore annihilation in a single-crystal nickel-base superalloy during hot isostatic pressing: Experiment and modelling, Mater. Sci. Eng. A. 586 (2013) 342–349. https://doi.org/10.1016/j.msea.2013.08.034.
[36] J.R. Poulin, A. Kreitcberg, V. Brailovski, Effect of hot isostatic pressing of laser powder bed fused Inconel 625 with purposely induced defects on the residual porosity and fatigue crack propagation behavior, Addit. Manuf. 47 (2021) 102324. https://doi.org/10.1016/j.addma.2021.102324.
[37] A. du Plessis, E. Macdonald, Hot isostatic pressing in metal additive manufacturing: X-ray tomography reveals details of pore closure, Addit. Manuf. 34 (2020) 101191. https://doi.org/10.1016/j.addma.2020.101191.
[38] H. Zhang, C. Li, G. Yao, Y. Zhang, Hot isostatic pressing of laser powder-bed-fused 304L stainless steel under different temperatures, Int. J. Mech. Sci. 226 (2022) 107413. https://doi.org/10.1016/j.ijmecsci.2022.107413.
[39] F.F. Conde, J.D. Escobar, J.P. Oliveira, M. Béreš, A.L. Jardini, W.W. Bose, J.A. Avila, Effect of thermal cycling and aging stages on the microstructure and bending strength of a selective laser melted 300-grade maraging steel, Mater. Sci. Eng. A. 758 (2019) 192–201. https://doi.org/10.1016/j.msea.2019.03.129.
[40] L. Kučerová, K. Burdová, Š. Jeníček, I. Chena, Effect of solution annealing and precipitation hardening at 250 °C–550 °C on microstructure and mechanical properties of additively manufactured 1.2709 maraging steel, Mater. Sci. Eng. A. 814 (2021). https://doi.org/10.1016/j.msea.2021.141195.